Interaction of polymer-coated silicon nanocrystals with lipid bilayers and surfactant interfaces

Ahmed Elbaradei, Samuel L. Brown, Joseph B. Miller, Sylvio May, and Erik K. Hobbie

Phys. Rev. E **94**, 042804 — Published 6 October 2016

DOI: 10.1103/PhysRevE.94.042804

Interaction of PEGylated Silicon Nanocrystals with Lipid Bilayers and Surfactant Interfaces

Ahmed Elbaradei, Samuel L. Brown, Joseph B. Miller, Sylvio May, and Erik K. Hobbie*

North Dakota State University, Fargo, North Dakota 58108

(Dated: July 28, 2016)

Abstract

We use photoluminescence (PL) microscopy to measure the interaction between PEGylated silicon nanocrystals (SiNCs) and two model surfaces; lipid bilayers and surfactant interfaces. By characterizing the photostability, transport, and size-dependent emission of the PEGylated nanocrystal clusters, we demonstrate the retention of red PL suitable for detection and tracking with minimal blueshift after a year in an aqueous environment. The predominant interaction measured for both interfaces is short-range repulsion, consistent with the ideal behavior anticipated for PEGylated phospholipid coatings. However, we also observe unanticipated attractive behavior in a small number of scenarios for both interfaces. We attribute this anomaly to defective PEG coverage on a subset of the clusters, suggesting a possible strategy for enhancing cellular uptake by controlling the homogeneity of the PEG corona. In both scenarios, the shape of the apparent potential is modeled through the free or bound diffusion of the clusters near the confining interface.

PACS numbers: 68.05.Gh, 81.07.Bc, 87.14.Cc, 87.16.D-

I. INTRODUCTION

Colloidal nanoparticles show considerable promise for a variety of potential applications in medicine and biomedical engineering, from imaging and drug delivery to thermal therapeutics and sensing [1]. Fluorescent nanoparticles, in particular, offer a unique platform for labeling and detection across a range of biologically relevant settings [2], with perhaps the most highly touted class of such materials being the semiconductor nanocrystals [3, 4]. In comparison to more traditional small-molecule fluorophores, colloidal quantum dots offer broad color tunability and improved photostability coupled with convenient access to a variety of relevant functionalities [5, 6]. However, concerns about the potential toxicity of many such materials [3, 4] are generating a significant amount of interest focused on finding nontoxic alternatives. At the same time, the emergence of colloidal nanocrystals for a variety of applications – flat-panel displays, solid-state lighting, and photovoltaics – ensures that they are poised to enter the environment, yet many questions about their impact remain unresolved [7].

In the context of such concerns, silicon is a particularly appealing material [8–10]. Silicon currently dominates the microelectronics industry but has achieved limited success in the realm of photonics, in part because of relatively poor bulk optical characteristics (*e.g.*, weak photoluminescence, indirect bandgap). At the nanoscale, however, the emission characteristics of silicon are greatly enhanced by changes in band structure imposed by quantum confinement, and a variety of routes to hydrophilic colloidal silicon nanocrystals (SiNCs) have emerged in just the past few years [11–21]. Although many of these provide broad color access with bright emission and single-particle dispersion, polyethylene glycol (PEG) remains the coating of choice [22]. For both drug-delivery and imaging, PEG reduces reticuloendothelial uptake and the potential for association with nontargeted sites. In addition to this 'stealth' effect [23], the chain structure of PEG reduces the impact of electrostatic interactions, while the ethylene glycol monomer improves solubility in a variety of relevant settings. Permeability and retention can be further modulated through the size of the polymer 'corona', while 'PEGylated' nanoparticles have been shown to exhibit low liver accumulation coupled with a high degree of tumor targeting [22]. Perhaps most importantly, PEG is inexpensive and FDA-approved for numerous applications, while a potential drawback is that PEGylation creates aggregates as opposed to fully dispersed individual nanocrystals.

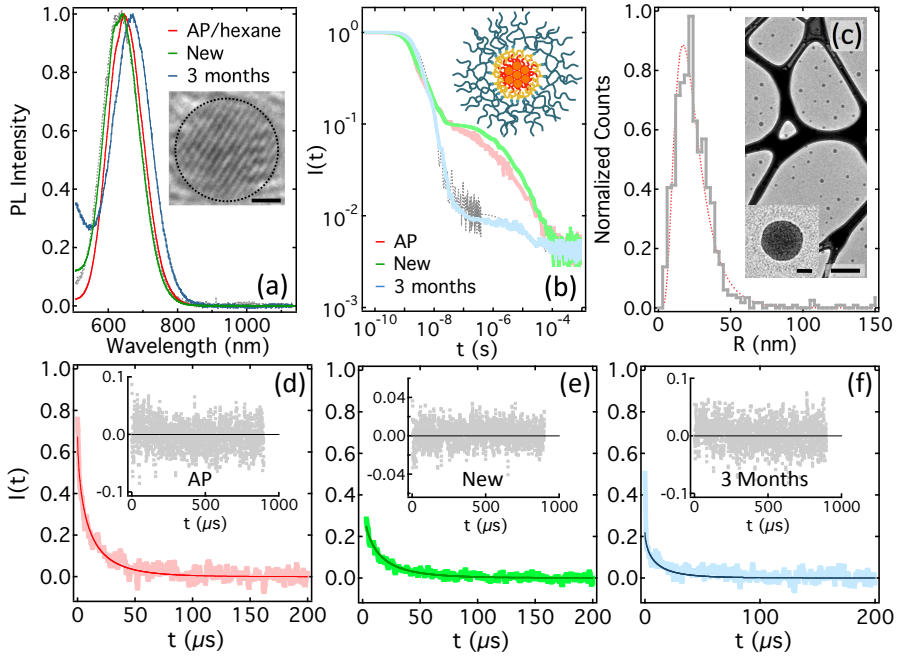

FIG. 1. (color online) (a) PL spectra of the AP material in hexane, and immediately ('New') and 3 months after PEGylation. The gray curve represents a sample after roughly 1 y. The inset shows a TEM image of an individual SiNC (scale = 1 nm). (b) PL relaxation in response to ps UV excitation for the same scenarios in the previous panel. The inset shows a schematic of a cluster (core = SiNCs, inner corona = lipid, outer corona = PEG). (c) TEM cluster-size distribution with log-normal representation (dashed curve). The main TEM image shows several clusters (500 nm scale) and the inset TEM image is a single cluster (50 nm scale). (d) Stretched-exponential fit and residual (inset) for the slow PL relaxation of AP, (e) 'New', and (f) '3 months'.

With the burgeoning interest in nanoparticles, a precise understanding of their cellular uptake commands considerable current attention [24]. Given the intrinsic complexity of biological cells, several recent studies employ lipid bilayers as model systems [25–36], particularly giant unilamellar vesicles (GUVs) [37–45]. While many such studies demonstrate nanoparticle uptake, much of the focus has been on structural changes in the bilayer mediated by nanoparticle interactions, with some studies implicating surface charge [37, 42] and others implicating hydrophobic/hydrophilic interactions [39, 43–45]. For example, recent studies of carboxylate-modified nanoparticles reveal two distinct internalization pathways [46], where an intrinsic attraction between the nanoparticle and the bilayer is a critical first element. However, very little scrutiny has been directed at pure PEG in this regard, pre-

sumably because of the assumed lack of interaction implicit in improved 'stealth'. Questions nonetheless persist about the uptake of nanoparticles with a pure-PEG corona [47, 48].

In general, mesoscale colloidal interactions in complex fluids are a topic of considerable current interest [49–58]. Here, we present a photoluminescence-based study of the interaction between PEGylated SiNCs and two model interfaces of generic importance to soft matter and biological physics; water-in-oil emulsions to simulate the hydrophobic/hydrophilic interface and GUVs for the barest physical representation of a cell. After quantifying the photostability, transport, and size-dependent emission of the PEGylated SiNC clusters in an aqueous environment, we turn our attention to the nature of the interaction with the two interfaces. We find predominantly short-range repulsive behavior for both, consistent with the prevailing view of pure PEG as a neutral/stable biocompatible surface. However, an unanticipated attractive behavior is also observed in a small number of scenarios, which we attribute to defective PEGylation on a subset of the clusters. This observation, in turn, suggests a possible strategy for enhancing cellular uptake through the homogeneity of a pure-PEG corona. In both scenarios, the shape of the apparent potential is modeled through the observed free or bound diffusion of the clusters, either inside the confining body or on the confining interface.

MATERIALS AND METHODS

The SiNCs were synthesized in a nonthermal low-pressure plasma and stabilized through liquid-phase thermal hydrosilylation in a 5:1 mixture of mesitylene and 1-dodecene [59]. The covalently bound ligand (1-dodecene) imparts colloidal stability in organic solvents while passivating the nanocrystal surface to improve photoluminescence (PL). Transmission electron microscopy (TEM) and X-ray diffraction suggest a mean SiNC diameter of 3.5 nm. Immediately after synthesis, the starting (AP) material in hexane exhibited a fluorescence quantum yield of 25 % and peak emission at 700 nm. Although the SiNCs were stored in a glovebox under a nitrogen atmosphere, the PL weakly blue-shifted over time, consistent with slight oxidation.

In general, SiNCs are PEGylated through incorporation into a PEG-phospholipid micelle, which produces water-soluble SiNC clusters [60]. Here, PEG-grafted phospholipids from Avanti Lipids [1,2-dimyristoyl-sn-glycero-3-phosphoethanolamine-N-[methoxy(polyethylene glycol)-2000] were dissolved in chloroform at 0.025 M. A 270 μL volume of 0.1 % SiNCs in

chloroform was placed in a 2 mL vial with 200 μL of the PEGylated phospholipid solution, and 330 μL of chloroform was added while stirring the mixture. The solution was then moved to a 50 mL round-bottom flask in a Buchi rotary evaporator (40 rpm for 2-3 h) and the solvent removed under vacuum. The flask was removed and hydrated with 2 mL of distilled water and allowed to sit overnight. Larger aggregates were then removed *via* centrifugation (Eppendorf 5424, 5000 rpm).

The GUVs were synthesized through 'gentle hydration' [61]. A 9:1 mixture of L-α-phosphatidylcholine/L-α-phosphatidylglycerol (PC/PG) was prepared in chloroform, and chloroform and methanol were then added at a 2:1 ratio, respectively, to yield 100 μL. The mixture was hand stirred in a glass vial for 5 min and then placed in a round-bottom flask, where it was dried by manual rotation under pure nitrogen at a 45 degree angle for 4-5 minutes. Finally, 1-2 ml of the PEGylated SiNC solution was added and the mixture was stored overnight at 37 °C. Water-in-oil emulsions were synthesized using sorbitan monostearate (Span 60) [62], which has a hydrophilic-lipophilic balance (HLB) of 4.7 and is soluble in toluene. A solution of 0.5 % of Span 60 in 2 mL of toluene was stirred for 2 min by hand, at which point 50 μL of the PEGylated SiNC solution was added to 500 μL of the toluene solution and the mixture was stirred for 2 min. In both cases, the aqueous phase contained the PEGylated SiNC clusters, which were thus found exclusively inside the emulsions but both inside/outside the GUVs. Samples were contained between two glass coverslips separated with a thin bead of vacuum grease and the slides were gently pushed together to seal the cell, which was then surveyed with PL microscopy until bodies containing a sufficiently dilute number of clusters (around 1-3 per body) were located for subsequent measurement.

PL imaging and spectroscopy were performed on a customized inverted microscope using a 60× 1.2 NA water-immersion objective. A Princeton ProEM 512B EMCCD with an X-Cite 120Q (120 W) excitation source was used for time-resolved video imaging, where a dim broadband visible lamp was introduced as background to allow detection of the GUV or emulsion interface. For lifetime measurements, modulated pulsed excitation was delivered with a fiber-coupled pulsed UV laser (Advanced Laser Diode Systems, PiL037, 375 nm, 30 ps pulse width, 140 mW peak power, 1 kHz to 1 MHz modulation) fiber coupled to a photomultiplier tube (Hamamatsu H10721-20) and recorded on a digital oscilloscope. PL spectra were measured in transmission on an upright microscope with a 4× long-working-distance NA 0.13 objective with a collimated 1mW fiber-coupled LED (365 nm) for excitation.

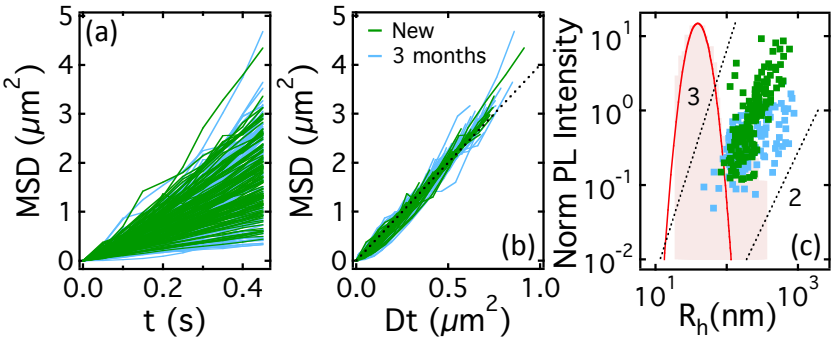

FIG. 2. (color online) (a) MSD *vs*. time for free clusters in water immediately ('New') and 3 months after PEGylation. (b) The same plot with time scaled by the diffusion coefficient, D. (c) Normalized PL intensity plotted against R_h for the two scenarios. The results are superimposed on the hydrodynamic size distribution extrapolated from TEM (shaded area) and the corresponding log-normal fit (curve). The two lines depict R_h^3 and R_h^2 behavior.

Transmission-electron microscopy (TEM) images were taken with a JEOL JEM-2100 analytical TEM operated at 200 kV using a GATAN Orius SC1000 bottom-mount CCD. The SiNCs were drop cast onto a holey carbon grid.

II. RESULTS AND DISCUSSION

Changes in PL with PEGylation and the size distribution of the SiNC-cluster core are detailed in Fig. 1. Immediately, there is little change ('New', Fig. 1a-b). Like the AP material, PEGylated SiNCs exhibit both 'fast' and 'slow' PL relaxation (Fig. 1b), where the fast (ns) relaxation has been linked to surface states [64] while the PL quantum yield is dominated by the slow (μs) mode [65, 66]. Here, the fast decay is around 4 ns independent of sample, with a slow decay of around 10 μs. After 3 months in water, the PL is red-shifted with respect to the AP material (blue curve, Fig. 1a), with an increase in the amplitude of the fast decay. This behavior was reproducible, although the precise shifts varied. The impact of oxidation on the PL of monodisperse SiNCs is well documented [67], but a red-shift accompanied by a decrease in emission intensity has been associated with nanocrystal aggregation in aqueous environments [68–72]. The gray curves in Fig. 1a-b represent a sample roughly 1 y after PEGylation, demonstrating a degree of long-term photostability. The inset to Fig. 1b shows a schematic of a PEGylated cluster, while the inset to Fig. 1c shows TEM images of the clusters. The cluster-size distribution based on TEM (Fig. 1c) is

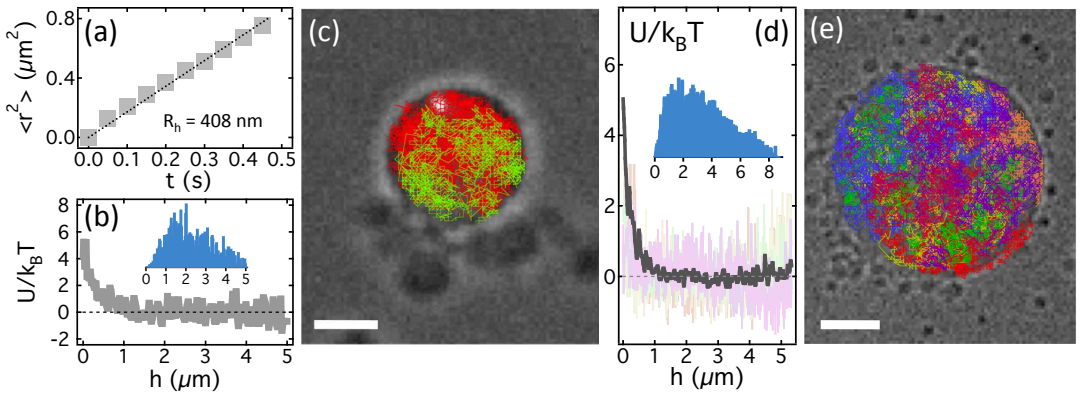

FIG. 3. (color online) (a) Time-dependent MSD used to extract R_h for a PEGylated SiNC cluster diffusing inside a water-in-oil emulsion. (b) Repulsive potential *vs*. radial distance from the interface as deduced from the long-time trajectory, where the inset shows the raw histogram. (c) Trajectory for the previous two panels (5 μm scale), where the time step is 0.05 s for a total of 14,321 (red) and 4073 (green) steps. (d) Analogous potential for a larger cluster/emulsion scenario (R_h = 800 nm), with the color-coded contribution of each 500 s interval shown in the background. The raw histogram is shown in the inset. (e) Superposed bright-field/PL image with the cluster trajectory (5 μm scale) for a total of 5 min, where each color represents a separate 500 s interval.

log-normal; $A \exp\{-[ln(R/R_p)/w]^2\}$ with $A = 0.89$, $R_p = 17$ nm, and $w = 0.7$, where R is cluster radius. The mean is 24.5 nm (4-5 nanocrystals, accounting for the ligand shell) with polydispersity index $\langle R^2\rangle/\langle R\rangle^2 = 1.28$.

To assess the stability of the PL quantum yield, the slow component of PL relaxation was fit to a stretched exponential of the form [65, 66]

$$I(t) = I_0 + A_2 \exp\left[-(t/\tau_2)^{\alpha_2}\right] \tag{1}$$

as shown in Fig. 1d-f. The relevant fitting parameters are $\alpha_2 = 0.65$ with $\tau_2 = 10.4$ μs (AP), $\alpha_2 = 0.65$ with $\tau_2 = 10.4$ μs ('New'), and $\alpha_2 = 0.65$ with $\tau_2 = 8.4$ μs ('3 months'). After fitting, the data were 'smoothed' with a binomial algorithm in IgorPro and the residuals were computed. Stretched-exponential relaxation is common in condensed-matter systems with disorder. Here, it reflect the combined effects of size polydispersity [65] and PL spectral linewidth, which is broadened by electron-phonon coupling in an indirect band-gap semiconductor [66]. The drop in PL lifetime after an extended time in water reflects a gradual decrease in quantum yield [67].

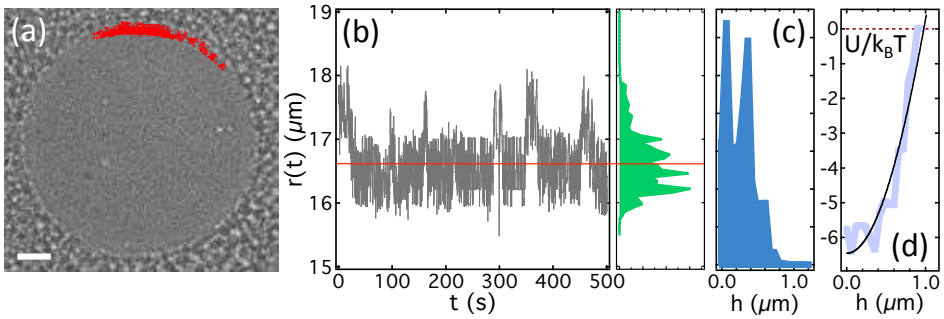

FIG. 4. (color online) (a) Superposed micrograph and trajectory of a cluster ($R_h \approx 450$ nm) diffusing near the interface of a water-in-oil emulsion over a 500 s interval (5 μm scale). (b) Radial position of the cluster *vs*. time, where the red line indicates the measured interface and the adjacent plot on the right shows the radial histogram based on the entire interval. (c) Raw histogram of the radial separation between the cluster and the interface, and (d) the corresponding attractive potential.

We first characterize the diffusion of free PEGylated SiNC clusters through PL-based tracking. Figure 2 shows the mean-square displacement (MSD) *vs*. time for cluster ensembles, both immediately after PEGylation ('New', 152 clusters) and after an extended time in water ('3 months', 142 clusters). From the linear relationships, we extract a diffusion coefficient D (Fig. 2b) through $\langle \mathbf{r}^2 \rangle = 4Dt$, where this analysis has been carried out for each individual cluster. The corresponding hydrodynamic radius, R_h, is then obtained through the Stokes-Einstein equation; $D = k_B T/6\pi R_h \eta$ where η is the viscosity of the suspending fluid. To determine η, we tracked the largest clusters of clearly discernible size in bright-field video microscopy, with an inversion of the Stokes-Einstein relation giving $\eta = 1.27$ mPa for 'New' and $\eta = 1.16$ mPa for '3 months', where both values are slightly above the viscosity of pure water.

The hydrodynamic radii are plotted in Fig. 2c with the normalized PL intensity of the cluster; $(I - I_b)/I_b$, where I is the maximum PL intensity and I_b is the background. The mean value of the optically measured R_h for freely diffusing clusters is 250 nm regardless of age. For comparison, the TEM distribution - with 20 nm added to the core radius to account for the PEG corona in the brush regime [72, 73] - is also shown. Although our optical setup can resolve the time dependent PL 'blinking' of an individual SiNC at a static position [74], the space-time PL signal of a diffusing particle in an aqueous environment is more challeng-

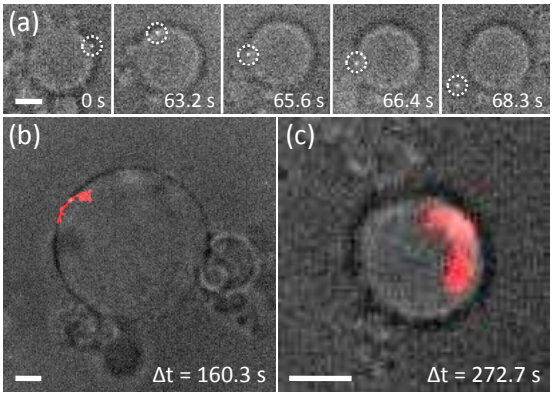

FIG. 5. (color online) (a) Superposed bright-field/PL image sequence of a PEGylated SiNC cluster initially adhered to the outside of a GUV that detaches (near $t = 67$ s) as the vesicle moves. We estimate a hydrodynamic radius of 400 nm based on the intensity trends in Fig. 2. (b) Superposed bright-field/PL time sequence of a PEGylated SiNC cluster (red) diffusing on the surface of a GUV, with a hydrodynamic radius of 300 nm based on the data in Fig. 2. (c) A similar image sequence for diffusion inside a GUV. In (b) and (c), a time sequence of PL images is summed to map the trajectory. The scale bar in each image is 5 μm.

ing to resolve. Here, our optical window starts near the peak of the TEM distribution (22 nm SiNC-cluster core radius) and extends up to the microscale. The detrimental effects of the aqueous environment are evident in the intensity *vs.* size trends, where the 'New' data scale as R_h^3, while the older data show a weaker dependence.

Turning to the influence of an interface, we consider the restricted diffusion of the clusters inside and on the interface of two distinct soft bodies; water-in-oil emulsions to model the hydrophobic/hydrophilic interface and GUVs as a bare representation of a cell membrane. To resolve the interface and track the confining body, we introduced a weak bright-field background, which favors the resolution of larger, brighter clusters. The measurements are a quasi-2D slice of 3D diffusion, where the resolved depth (z_0, defined below) is dictated by the optics and the PL intensity of the cluster. Under typical conditions, we measured $z_0 \approx 4$ μm. The signal disappears when the cluster moves outside of this slice and a time-linear interpolation scheme was used to 'splice' the respective data sets. To characterize the interaction, we positioned the focal plane near the equatorial plane of the confining body and recorded the motion of a cluster inside.

We focus first on emulsions. Unless the cluster is bound to the interface, the size can be

obtained from a Stokes-Einstein analysis of the early-time diffusion (Fig. 5a), although it can also be roughly interpolated from the PL intensity and Fig. 2c. To define an effective potential, we construct a histogram, $N(h)$, of the clusters radial distance h from the confining interface through the measured diameter and centroid of the confining body (insets, Fig. 3b,d). Defining the probability $p(h) = N(h)/[2\pi N_{tot}(R_0 - h)]$, where N_{tot} is the total number of diffusion steps and R_0 is the radius of the cavity, we define an apparent potential through a Boltzmann factor; $U(h) = -k_B T \ln(p)$, where $k_B T$ is the thermal energy. This quasi-2D analysis accounts for a larger diffusion volume near the interface, away from the center of the body. We show two separate examples of this in Fig. 3 based on the tracking of single clusters inside two different emulsions. In both cases, the potential appears as a 'soft' repulsion but is indicative of an essentially hard-sphere interaction with the interface; the range is an artifact of confinement, as we demonstrate below. Figure 3 uses color to highlight the trajectories of different subintervals in a typical dataset. In Fig. 3c, the total time interval is just over 15 minutes, but one 3.5 min subinterval is highlighted in green. We take this one step further Fig. 3e, which color codes each 500 s subinterval of a 5 min dataset. Displaying the data in this manner provides a better sense of the dynamic range of cluster motion, which would otherwise be obscured by the large number of steps.

Surprisingly, the interaction was found to be attractive on occasion (Fig. 4). Figure 4b shows the radial position of a cluster (with respect to the centroid of the emulsion) *vs.* time, where the red horizontal line is the location of the interface measured from the micrograph. The right panel of Fig. 4b shows a histogram of this behavior, where the peaks reflect the discrete pixelated nature of the trajectory (1 pixel = 266.7 nm). In this instance, the focal and equatorial planes are slightly mismatched, with the cluster appearing to move beyond the apparent interface of the confining body. Defining the cutoff by the red line, we get $p(h)$ and the apparent potential (Fig. 4d). The range of attraction is again an artifact of confinement. Of the 13 emulsion/cluster pairs that we analyzed in detail, 3 exhibited attractive behavior. However, the requirements for tracking clusters within emulsions were rather stringent (1-3 clusters, uniform shape, limited emulsion motion, long observation window), implying that the search for such bodies was somewhat subjective. A more meaningful analysis based on the video observation of a large number of emulsions suggested attractive behavior in 4 out 38 (~ 10 %). With the inclusion of larger clusters beyond the size window in Fig. 2, this increased slightly to 8 out of 42. Although this suggests an increased tendency

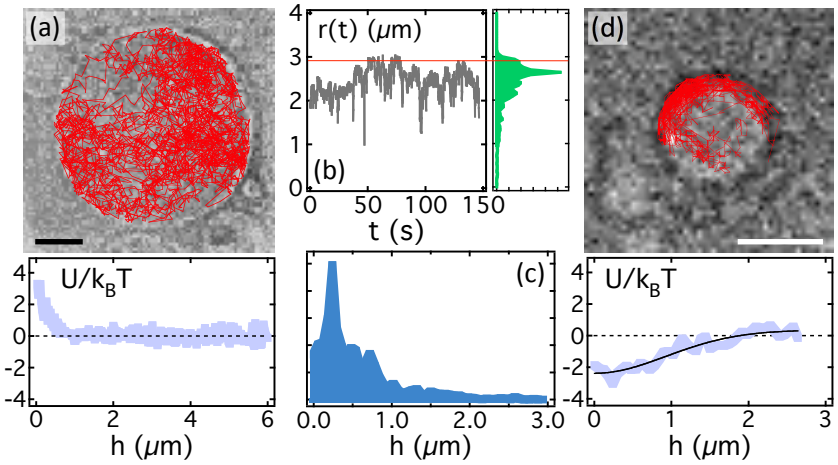

FIG. 6. (color online) (a) Superposed micrograph and trajectory of a PEGylated SiNC particle diffusing inside a GUV showing hard-sphere repulsive behavior with the membrane (top) and the corresponding potential (bottom). Based on intensity, we estimate a hydrodynamics radius of 150 nm from Fig. 2. (b) Time dependent radial position and average radial histogram for a particle diffusing in a GUV with attractive behavior, where we estimate a hydrodynamic radius of 350 nm based on PL intensity. The red line is the measured position of the interface. (c) Raw histogram of the radial separation between the particle and the interface in (b), and (d) micrograph of the GUV with superposed particle trajectory (top) and the corresponding attractive potential (bottom). The scale bar in each image is 5 μm.

for attraction with larger cluster size, the results are not statistically significant.

Turning to lipid bilayers, the majority of interactions were again repulsive, but with measurable exceptions. Although we only quantified the interaction for clusters confined within GUVs, Fig. 5a shows a time sequence of a cluster adhered to the external surface of a GUV. After roughly 1 min of observation, smaller GUVs diffuse into the field of view and cause the body to move and rotate, and we eventually observe the cluster break free. We show this sequence because it clearly demonstrates the existence of attractive behavior. More relevant to the measured interactions, Fig. 5b depicts the diffusion of a cluster on an inner GUV surface, while Fig. 5c depicts a cluster diffusing within the bulk of a GUV, where both images are a superposition of a static bright-field frame (gray background) and a summed PL image sequence (bright). Representative potentials for GUVs measured using our particle tracking approach are shown in Fig. 6. Of the 11 GUVs that we analyzed in detail, 3 showed attractive behavior. Again, video observation provides a more meaningful

statistic, with attractive behavior in 2 out of 38 GUVs (~ 5 %) and a slightly higher number (4 out of 40) if larger clusters (beyond the range of Fig. 2) are included.

To explain the shape of U, we note that there is no physical mechanism in either system for long-range repulsion/attraction. Although smaller micelles could potentially mediate attractive depletion interactions, the concentration of such micelles is low. We thus model U through geometrical effects associated with confinement, assuming either short-range repulsion through excluded volume or short-range attraction through hydrophobic/hydrophilic interactions. We consider a spherical vesicle/emulsion of radius R_0, centered at the origin of a cylindrical coordinate system (Fig. 7a). A small colloid diffuses either inside or on the surface and is observed along the z-axis within $-z_0 < z < z_0$. The 2D-projection of the observed trajectory gives rise to the apparent potential $U(r)$, where r is the distance from the z-axis, that is non-vanishing for $r_0 < r < R_0$ with $r_0 = \sqrt{R_0^2 - z_0^2}$.

The volume and area of the observable section of the vesicle are

$$V(z_0) = 2\pi \int_0^{R_0} dr\, r\, v(r) = 2\pi z_0 \left(R_0^2 - \frac{z_0^2}{3} \right),$$
$$A(z_0) = 2\pi \int_0^{R_0} dr\, r\, a(r) = 4\pi R z_0, \tag{2}$$

where $v(r) = 2\sqrt{R_0^2 - r^2}$ for $r > r_0$, $v(r) = 2z_0$ for $r < r_0$, $a(r) = 2R_0/\sqrt{R_0^2 - r^2}$ for $r > r_0$, and $a(r) = 0$ for $r < r_0$. We recover $V(z_0 = R_0) = 4\pi R_0^3/3$ and $A(z_0 = R_0) = 4\pi R_0^2$ if the entire vesicle is observed, and $V(z_0 \ll R_0) = 2\pi z_0 R_0^2$ for a thin slice. We define probabilities $p_V(r)$ and $p_A(r)$ to find the particle in V or on A, respectively, a distance r from the z-axis. Both probabilities are normalized as

$$\frac{2}{R_0^2} \int_0^{R_0} dr\, r\, p_i(r) = 1 \tag{3}$$

and are easily determined to be

$$p_V(r) = \begin{cases} \frac{R_0}{z_0} \frac{\sqrt{1-(r/R_0)^2}}{1-z_0^2/(3R_0^2)} & \text{if } r > r_0, \\ \frac{1}{1-z_0^2/(3R_0^2)} & \text{if } r < r_0, \end{cases} \tag{4}$$

and

$$p_A(r) = \begin{cases} \frac{R_0}{2z_0\sqrt{1-(r/R_0)^2}} & \text{if } r > r_0, \\ 0 & \text{if } r < r_0. \end{cases} \tag{5}$$

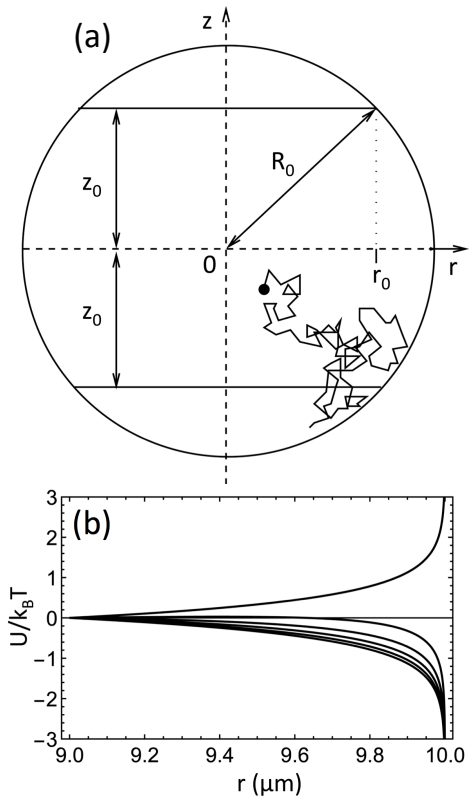

FIG. 7. (a) Schematic illustration of a spherical vesicle of radius R_0. Only a region of thickness $2z_0$ is observed. (b) $U(r)$ (in units of k_BT) according to Eq. (6) for $R_0 = 10\,\mu$m and $z_0 = 4.36\,\mu$m. The six different curves correspond to $\phi_A = 0$, 0.2, 0.4, 0.6, 0.8, and 1.0. (from top to bottom).

The colloid is bound to the interface with probability ϕ_A ($0 \leq \phi_A \leq 1$) with probability $\phi_V = 1 - \phi_A$ for being in the volume. The total probability $p(r) = \phi_V p_V(r) + \phi_A p_A(r)$ defines the apparent interaction potential $U(r) = -k_BT \ln p(r)$ as

$$\frac{U(r)}{k_BT} = -\ln\left[(1-\phi_A)\frac{R_0}{z_0}\,\frac{\sqrt{1-(r/R_0)^2}}{1-z_0^2/(3R_0^2)} + \phi_A \frac{R_0}{2z_0\sqrt{1-(r/R_0)^2}}\right]. \tag{6}$$

Note that $U(r)$ diverges as $r \to R_0$, either to $U(r \to R) \to +\infty$ for $\phi_A = 0$ or to $U(r \to R) \to -\infty$ for $\phi_A > 0$. The divergence to $+\infty$ reflects a vanishing number of states at $r = R_0$ if diffusion is in the volume. The divergence to $-\infty$ arises from a diverging number of states at $r = R_0$ if diffusion is on the surface. There are three parameters; R_0, z_0, and ϕ_A, as shown in Fig. 7b for different ϕ_A.

A schematic of the interaction of a cluster with a GUV is shown in Fig. 8a-b, which can be generalized to emulsions by replacing the lipid bilayer with a Span60 water-oil interface.

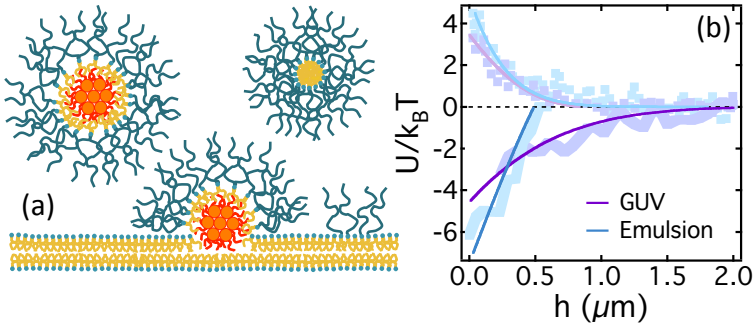

FIG. 8. (color online) (a) Schematic of the interaction showing a stable cluster, a bound cluster and a pure PEG micelle. (b) Agreement between the measured and predicted trends for the apparent potentials. Repulsive and attractive behavior is presented for both emulsion and GUV interactions. The main contributors to radial structure in U are the size of the GUV/emulsion, and fluctuations in radial position due to factors detailed in the text.

For simplicity – and in light of resolution issues related to tracking a cluster near a curved interface – we limit our analysis to either pure repulsion ($\phi_A = 0$) or pure attraction ($\phi_A = 1$). In realty, however, attractive clusters likely detach and reattach to the interface over longer time intervals. For pure repulsion ($\phi_A = 0$), the apparent range of U is an artifact of confinement; clusters slightly displaced from the equator but within the depth of resolution will appear to be repelled at a radial distance smaller than R_0. Figure 8c shows fits of the repulsive potentials in Figs. 3 and 6 by convolving Eq. (6) ($\phi_A = 0$) with a 500 nm Gaussian using the measured radius of the vesicle. In the attractive case ($\phi_A = 1$), confinement of the particle both at the interface and near the equator creates a histogram more susceptible to 'noise' (*e.g.*, focal/equatorial mismatch, nonspherical vesicle shape) because the cluster exhibits less motion. In the attractive scenarios of Fig. 4 and 6, the combined spread in the location of the interface approaches 1 μm. Convoluting the expression for $U(\phi_A = 1)$ with a 1 μm Gaussian and adjusting the position of $h = 0$ in accord with this uncertainty, we can model the shape of the apparent potentials (Fig. 8c). The finite range of the attraction originates from the bound aggregate moving up/down the interface, limited by uncertainty in h. The difference in the apparent range of attraction between emulsion (Fig. 4) and GUV (Fig. 6) is a reflection of the difference in size. In both cases, the true potential is a short-range attraction.

CONCLUSIONS

We offer insight into the photo-physical fate of PEGylated SiNCs in aqueous, biologically relevant settings. Although measurable spectral change occured over the span of a month to a year, the SiNC clusters retained their characteristic red PL with sufficient intensity for optical detection and tracking down to the 50 nm scale after 1 year in water. We have also measured and characterized the apparent interaction potential between the PEGylated SiNC clusters and two generic surfaces of considerable importance to soft matter and biological physics; lipid bilayers and surfactant interfaces. Through what is sometimes referred to as the 'PEG dilemma', the long retention times associated with improved 'stealth' often come at the expense of poor cellular uptake due to the relatively neutral interaction of PEG with cell membranes [75]. Our measurements quantify and support this, but we also find an unanticipated attraction between the clusters and the interface in ~ 10 % of emulsions and ~ 5 % of GUVs. Although there is some suggestion that larger clusters are more likely to be attracted to the interface, such data are limited and not statistically significant. Beyond a number of minor factors that impact the apparent range of the interaction, the predominant influence is the size of the confining body.

Overall, our findings support a picture of neutral interactions between PEGylated SiNC clusters and lipid bilayers or surfactant interfaces. This suggests that the uptake of nanoparticles with pure PEGylated-phospholipid coronas depends critically on the presence of other components, such as proteins [75]. When attraction does occur, it could be explained by 'defects' or 'patches' of below-average PEG coverage that have reduced hydrophilicity and hence a natural affinity for the interface [76]. Although uncommon in this study, the occurrence of attractive behavior is noteworthy because it suggests potential strategies for controlling cellular uptake by engineering 'patchiness' through precise control over heterogeneities in the PEG coating.

ACKNOWLEDGEMENTS

We thank Rebecca Anthony and Uwe Kortshagen for providing the nanocrystals. The authors acknowledge the support of the National Science Foundation (NSF) through CBET-1133135.

[1] T. L. Doane, C. Burda, *Chem. Soc. Rev.* **41**, 2885 (2012).

[2] W. Zhong, *Anal. Bioanal. Chem.* **394**, 47 (2009).

[3] K.-T. Yong, W.-C. Law, C. Hu, L. Ye, L. Liu, M. T. Swihart, P. N. Prasad, *Chem. Soc. Rev.* **42**, 1236 (2013).

[4] Y. Wang, R. Hu, G. Lin, I. Roy, K.-T. Yong, *ACS Applied Mater. Int.* **5**, 2786 (2013).

[5] M. Bruchez, M. Moronne, P. Gin, S. Weiss, A. P. Alivisatos, *Science* **281**, 2013 (1998).

[6] J. F. Galloway, A. Winter, K. H. Lee, J. Park, C. Dvoracek, P. Devreotes, P. C. Searson, *Nanomedicine* **8**, 1190 (2012).

[7] Z. Nie, A. Petukhova, E. Kumacheva, *Nat. Nanotechnol.* **5**, 15 (2010).

[8] H. Jaganathan, B. Godin, *Adv. Drug Deliv. Rev.* **64**, 1800 (2012).

[9] F. Peng, Y. Su, Y. Zhong, C. Fan, S.-T. Lee, Y. He, *Accts. Chem. Res.* **47**, 612 (2014).

[10] See, for example, E. C. Wu, J. S. Andrew, L. Cheng, W. R. Freeman, L. Pearson, M. J. Sailor, *Biomaterials* **32**, 1957 (2010).

[11] A. Shiohara, S. Prabakar, A. Faramus, C.-Y. Hsu, P.-S. Lai, P. T. Northcote, R. D. Tilley, *Nanoscale* **3**, 3364 (2011).

[12] B. F. P. McVey, R. D. Tilley, *Accts. Chem. Res.* **47**, 3045 (2014).

[13] C. M. Hessel, M. R. Rasch, J. L. Hueso, B. W. Goodfellow, V. A. Akhavan, P. Puvanakrishnan, J. W. Tunnel, B. A. Korgel, *Small* **6**, 2026 (2010).

[14] Y. Zhong, F. Peng, F. Bao, S. Wang, X. Ji, L. Yang, Y. Su, S.-T. Lee, Y. He, *J. Am. Chem. Soc.* **135**, 8350 (2013).

[15] E. J. Henderson, A. J. Shuhendler, P. Prasad, V. Baumann, F. Maier-Flaig, D. Faulkner, U Lemmer, X. Y. Wu, G. A. Ozin, *Small* **7**, 2507 (2011).

[16] R. J. Clark, M. K. M. Dang, J. G. C. Veinot, *Langmuir* **26**, 15657 (2010).

[17] Y. He, Y. Zhong, F. Peng, X. Wei, Y. Su, Y. Lu, S. Su, W. Gu, L. Liao, S.-T. Lee, *J. Am. Chem. Soc.* **133**, 14192 (2011).

[18] H. Sugimoto, M. Fuji, Y. Fukuda, K. Imakita, K. Akamatsu, *Nanoscale* **6**, 122 (2014).

[19] K. K. Chen, K. Liao, G. Casillas, Y. Li, G. A. Ozin, *Adv. Sci.* **3**, DOI: 10.1002/advs.201500263 (2016).

[20] J. J. Wu, V. S. S. K. K. Kondeti, P. J. Bruggeman, U. R. Kortshagen, *J. Phys. D* **49**, 08LT02 (2016).

[21] S. Chandra, B. Ghosh, G. Beaune, U. Nagarajan, T. Yasui, J. Nakamura, T. Tsuruoka, Y. Baba, N. Shirahata, F. M. Winnik, *Nanoscale* **8**, 9009 (2016).

[22] J. V. Jokerst, T. Lobovkina, R. N. Zare, S. S. Gambhir, *Nanomedicine* **6**, 715 (2011).

[23] D. D. Lasic, D. Needham, *Chem. Rev.* **95**, 2601 (1995).

[24] L. W. Zhang, N. A. Monteiro-Riviere *Toxicol. Sci.* **110**, 138 (2009).

[25] L. Wu, X. Jiang, *Anal. Bioanal. Chem.* DOI 10.1007/s00216-015-9157-5 (2016).

[26] B. Lu, T. Smith, J. Schmidt, *Nanoscale* **7**, 7858 (2015).

[27] A. R. Mhashal, S. Roy, *PLoS One* **9**, e114152 (2014).

[28] C. M. Bailey, E. Kamaloo, K. L. Waterman, K. F. Wang, R. Nagarajan, T. A. Camesano, *Biophys. Chem.* **203-204**, 51 (2015).

[29] Y. Roiter, M. Ornatska, A. R. Rammohan, J. Balakrishnan, D. R. Heine, S. Minko, *Nano Lett.* **8**, 941 (2008).

[30] R. P. Carney, Y. Astier, T. M. Carney, K. Votchovsky, P. H. J. Silva, F. Stellacci, *ACS Nano* **7**, 932 (2013).

[31] A. E. Nel, L. Madler, D. Velegol, T. Xia, E. M. Hoek, P. Somasundaran, F. Klaessig, V. Castranova, M. Thompson, *Nat. Mater* **8**, 543 (2009).

[32] K. L. Chen, G. D. Bothun, *Environ. Sci. Technol.* **48**, 873 (2014).

[33] P. R. Leroueil, S. A. Berry, K. Duthie, G. Han, V. M. Rotello, D. Q. McNerny, J. R. Baker, B. J. Orr, M. M. Banaszak Holl, *Nano Lett.* **8**, 420 (2008).

[34] C. Peetla, V. Labhasetwar, *Langmuir* **25**, 2369 (2009).

[35] X. Xiao, G. A. Montao, T. L. Edwards, A. Allen, K. E. Achyuthan, R. Polsky, D. R. Wheeler, S. M. Brozik, *Langmuir* **28**, 17396 (2012).

[36] R. C. Van Lehn, M. Ricci, P. H. J. Silva, P. Andreozzi, J. Reguera, K. Votchovsky F. Stellacci, A. Alexander-Katz, *Nat Commun.* **5**, 4482 (2014).

[37] S. Li, N. Malmstadt, *Soft Matter* **9**, 4969 (2013).

[38] A. Dubavik, E. Sezgin, V. Lesnyak, N. Gaponik, P. Schwille, A. Eychmller, *ACS Nano* **6**, 2150 (2012).

[39] B. Jing, Y. Zhu, Y. *J. Am. Chem. Soc.* **133**, 10983 (2011).

[40] C. Montis, D. Maiolo, I. Alessandri, P. Bergese, D. Berti, *Nanoscale* **6**, 6452 (2014).

[41] A. Akesson, C. V. Lundgaard, N. Ehrlich, T. G. Pomorski, D. Stamou, M. Cardenas, *Soft Matter* **8**, 8972 (2012).

[42] S. Zhang, A. Nelson, P. A. Beales, *Langmuir* **28**, 12831 (2012).

[43] M. Laurencin, T. Georgelin, B. Malezieux, J.-M. Siaugue, C. Mnager, *Langmuir* **26**, 16025 (2010).

[44] R. C. Van Lehn, P. U. Atukorale, R. P. Carney, Y.-S. Yang, F. Stellacci, D. J. Irvine, A. Alexander-Katz, *Nano Lett.* **13**, 4060 (2010).

[45] B. Jing, R. C. T. Abot, Y. Zhu, *J. Phys. Chem. B* **118**, 13175 (2014).

[46] Y. Li, L. Shanga, G. U. Nienhaus, *Nanoscale* 10.1039/c6nr01495j (2015).

[47] T. A. Kelf, V. K. A. Sreenivasan, J. Sun, E. J. Kim, E. M. Goldys, A. V. Zvyagin, *Nanotechnology* **21**, 285105 (2010).

[48] A. Xi, G. D. Bothun, *Analyst* **139**, 973 (2014).

[49] M. D. Gratale, T. Still, C. Matyas, Z. S. Davidson, S. Lobel, P. J. Collings, A. G. Yodh, *Phys. Rev. E* **93**, 050601(R) (2016).

[50] Y. Galerne, *Phys. Rev. E* **93**, 042702 (2016).

[51] D. J. Evans, A. D. Hollingsworth, D. G. Grier, *Phys. Rev. E* **93**, 042612 (2016).

[52] D. W. Pilat, B. Pouligny, A. Best, T. A. Nick, R. Berger, H.-J. Butt, *Phys. Rev. E* **93**, 022608 (2016).

[53] H. S. Antila, P. R. Van Tassel, M. Sammalkorpi, *Phys. Rev. E* **93**, 022602 (2016).

[54] C. P. Kelleher, A. Wang, G. I. Guerrero-Garca, A. D. Hollingsworth, R. E. Guerra, B. J. Krishnatreya, D. G. Grier, V. N. Manoharan, P. M. Chaikin, *Phys. Rev. E* **92**, 062306 (2015).

[55] S. D. C. Pushpam, M. G. Basavaraj, E. Mani, *Phys. Rev. E* **92**, 052314 (2015).

[56] H. Carstensen, V. Kapaklis, M. Wolff, *Phys. Rev. E* **92**, 012303 (2015).

[57] A. V. Ryzhkova, M. Skarabot, I. Musevic, *Phys. Rev. E* **91**, 042505 (2015).

[58] I. Sriram, E. M. Furst, *Phys. Rev. E* **91**, 042303 (2015).

[59] R. J. Anthony, D. J. Rowe, M. Stein, J. Yang, U. Kortshagen, *Adv. Funct. Mater.* **21**, 4042 (2011).

[60] F. Erogbogbo, K. T. Yong, I. Roy, G. X. Xu, P. N. Prasad, M. T. Swihart *ACS Nano* textbf2, 873 (2008).

[61] J. P. Reeves, R. M. Dowben, *J. Cellular Physiology* **73**, 49 (1969).

[62] J. M. Williams, *Langmuir* **7**, 1370 (1991).

[63] F. Erogbogbo, K.-T. Yong, I. Roy, H. Hu, W.-Z Law, W. Zhao, H. Ding, F. Wu, R. Kumar, M. T. Swihart, P. N. Prasad, *ACS Nano* **5**, 413 (2011).

[64] Z. Yang, G. B. De los Reyes, L. V. Titova, I. Sychugov, M. Dasog, J. Linnros, F. A. Hegmann, J. G. C. Veinot, *ACS Photonics* 10.1021/acsphotonics.5b00143 (2015).

[65] J. B. Miller, A. R. Van Sickle, R. J. Anthony, D. M. Kroll, U. R. Kortshagen, E. K. Hobbie, *ACS Nano* **6**, 7389 (2012).

[66] A. R. Van Sickle, J. B. Miller, C. Moore, R. J. Anthony, U. R. Kortshagen, E. K. Hobbie, *ACS Appl. Mater. & Interfaces* **5**, 4233 (2013).

[67] M. L. Mastronardi, K. K. Chen, K Liao, G. Casillas, G. A. Ozin, *J. Phys. Chem C* **119**, 826 (2015).

[68] M. Ulusoy, R. Jonczyk, J.-G. Walter, S. Springer, A. Lavrentieva, F. Stahl, M. Green, T. Scheper, *Bioconj. Chem.* **27**, 414 (2016).

[69] W. Y. Huang, D. W. Bai, L. J. Li, H. D. Wei, Z. P. Shi, H. Cheng, Y. Q. Li, *J. Sol-Gel Sci. Technol.* **74**, 718 (2015).

[70] V. Poderys, M. Matulionyte, A. Selskis, R. Rotomskis, *Nanoscale Res. Lett.* **6**, 9740 (2011).

[71] H. Zhang, Z. Zhou, B. Yang, M. Y. Gao, *J. Phys. Chem. B* **107**, 8 (2003).

[72] B. Ashok, L. Arleth, R. P. Hjelm, I. Rubinstein, H. Onyuksel, *J. Pharm. Sci.* **93**, 2476 (2004).

[73] O. Tirosh, Y. Barenholz, J. Katzhendler, A. Priev, *Biophys. J.* **74**, 1371 (1998).

[74] J. B. Miller, N. Dandu, K. A. Velizhanin, R. J. Anthony, U. R. Kortshagen, D. M. Kroll, S. Kilina, E. K. Hobbie, *ACS Nano* **9**, 9772 (2015).

[75] D. Pozzi, V. Colapicchioni, G. Caracciolo, S. Piovesana, A. L. Capriotti, S. Palchetti, S. De Grossi, A. Riccioli, H. Amenitsch, A. Lagan, *Nanoscale* **6**, 2782 (2014).

[76] C. Bonnaud, C. A. Monnier, D. Demurtas, C. Jud, D. Vanhecke, X. Montet, R. Hovius, M. Lattuada, B. Rothen-Rutishauser, A. Petri-Fink, *ACS Nano* **8**, 3451 (2014).